International Journal of Biological Macromolecules 311 (2025) 143997

Contents lists available at ScienceDirect

International Journal of Biological Macromolecules

journal homepage: www.elsevier.com/locate/ijbiomac

Mussel-inspired multifunctional gelatin microgel for accelerating full-thickness wound healing

Lijing Teng [a,b,c,1], Honghong Zhang [a,b,1], Xiaomin Sun [a,b,c,1], Xinping Wang [a,b,c], Yeshuang Zhong [a,b,c], Simian Zhu [a,b,c], Xiangyu Zeng [a,b,c], Yu Dong [a,b,c], Zhu Zeng [a,b,*], Zhou Li [d,**], Qiang Zheng [a,b,c,*]

[a] School of Basic Medical Sciences/School of Biology and Engineering (School of Modern Industry for Health and Medicine), Guizhou Medical University, Guian New District, Guiyang 561113, China
[b] Key Laboratory of Biology and Medical Engineering, Guizhou Key Laboratory of Microbio and Infectious Disease Prevention & Control, Immune Cells and Antibody Engineering Research Center in University of Guizhou Province, Guizhou Medical University, Guian New District, Guiyang 561113, China
[c] Engineering Research Center of Intelligent Materials and Advanced Medical Devices, School of Biology and Engineering, Guizhou Medical University, Guian New District, Guiyang 561113, China
[d] Beijing Institute of Nanoenergy and Nanosystems Chinese Academy of Sciences, Beijing 101400, China

ARTICLE INFO

Keywords:
Microgels
Multifunction
Wound healing

ABSTRACT

The complete wound healing is challenging in clinical practice originating from bleeding, inflammation or infection, leading to poor healing process. Here, inspired by the mussel's adhesion, we successfully developed a polydopamine functionalized gelatin microgel (PGM) using a simple emulsification-chemical crosslinking technique, which method enables the controllable and facile generation of PGM, allowing for the facile production of PGM with different sizes (15–100 μm). PGM demonstrates remarkable adaptability to complex wound shapes and depths, ensuring stable tissue adhesion even in dynamic and moist microenvironment, the optimal adhesive strengths of PGM adhering to porcine skin is 10.3 kPa. Particularly, its multifunctional performance integrates cell migration, hemostatic activity, and reactive oxygen species scavenging. In addition, skin wound healing in a full-thickness skin defect model was achieved by down regulating TNF-*α* expression while promoting collagen regeneration and CD31 expression. Altogether, a new strategy of injectable microgel is developed for drug-free, efficient full-thickness wound healing, offering significant potential for clinical applications.

1. Introduction

Skin is the most vulnerable organ in body and is highly susceptible to damage from physical trauma or chemical stimuli, further resulting in both physical and mental impairment to patients [1]. Effective wound healing is a complex physiologic process that involves a sequential cascade of events, including hemostasis, inflammation, proliferation, and remodeling [2]. While some injuries display an intrinsic self-healing ability over time, adult skin injuries often fail to fully recover, typically leading to scarring and/or the loss of skin appendages [3]. Although various biomaterials with potent sustained release are widely utilized for wound repair and management, their cytotoxic and hemolytic effects, as well as the accumulation of reactive oxygen species (ROS), can exacerbate tissue damage [4]. In consequence, the development of drug-free bioactive dressings capable of stopping bleeding, modulating inflammation, and actively promoting tissue regeneration holds significant promise for achieving optimal wound healing [5,6].

Hydrogels are promising as wound dressings due to their biodegradability, biocompatibility, extracellular matrix (ECM)-like structure, and ability to offer a moist environment for healing [7–9]. Among them, injectable hydrogels are promising for the treatment of wound healing due to their fewer adverse effects, easier use, and minimally invasive delivery procedure, which can effectively bypass the inconvenience of surgery, displaying a better affinity to host tissue [10]. Despite

* Corresponding authors at: School of Basic Medical Sciences/School of Biology and Engineering (School of Modern Industry for Health and Medicine), Guizhou Medical University, Guian New District, Guiyang 561113, China.
** Corresponding author.
E-mail addresses: zengzhu@gmc.edu.cn (Z. Zeng), zli@binn.cas.cn (Z. Li), Zhengqiang@gmc.edu.cn (Q. Zheng).
[1] These authors contributed equally to this work.

https://doi.org/10.1016/j.ijbiomac.2025.143997
Received 4 March 2025; Received in revised form 19 April 2025; Accepted 5 May 2025
Available online 6 May 2025

substantial developments, injectable hydrogels usually swell and cannot hold their shape, which may exert pressure on the surrounding tissues, leading to edema-like conditions [11]. In addition, traditional injectable hydrogels are typically manufactured into a relatively large sizes with low surface/volume ratio, leading to poor cell ingrowth and tissue formation [12]. Furthermore, these bulk hydrogels possess only nanoporous structures within their insoluble network and lack micropores, resulting in inadequate nutrient exchange and low cell viability. Microgels, unlike traditional injectable hydrogels, exhibit improved injectability due to their uniform spherical shape and higher surface-to-volume ratio. In addition, the short diffusion distance is in favor of nutrient mass transport, thus enhancing long-term cell survival [13]. Moreover, the interconnected pores not only permit cellular ingrowth but also promote angiogenesis, ensuring collagen deposition and supporting tissue regeneration before the microgels degrade [14,15]. Simultaneously, combining bioactive molecule enables develop multifunctional microgel, such as hemostatic activity [16], reactive oxygen species scavenging [17], and inflammation modulation [18]. However, current multifunctional microgel fabrication methods suffer from their complexity and poor controllability. Current microgels are typically created using specialized microfluidic techniques, where hydrogel precursors are dispersed into individual microdroplets and subsequently crosslinked with ultraviolet light [19,20]. There are some challenges with these approaches [21]. For example, microfluidic technology necessitates costly capillary devices or microchannel chips, which are technically challenging in microgel development [22]. In addition, microfluidic devices usually lack a crosslinking strategy, as hydrogel microdroplets can only undergo cross-linking downstream, which may lead to fusion and instability. Finally, microgel formation usually requires surfactants such as liquid paraffin and Span 80, which can leave residual chemicals that may trigger biocompatibility issues [23]. Consequently, it is imperative for developing a novel method that guarantees facile and rapid operation, excellent biocompatibility, and bioactivity for fabricating microgels.

Here, we designed a mussel-inspired, multifunctional, drug-free and adaptive polydopamine functionalized gelatin microgel, denoted as PGM, for accelerating full thickness wound healing. As shown in Fig. 1, gelatin microgel (GM) was first developed by blending positively charged gelatin and negatively charged gum arabic to drive phase separation [24,25], in which FDA-approved Pluronic® F-127 was utilized

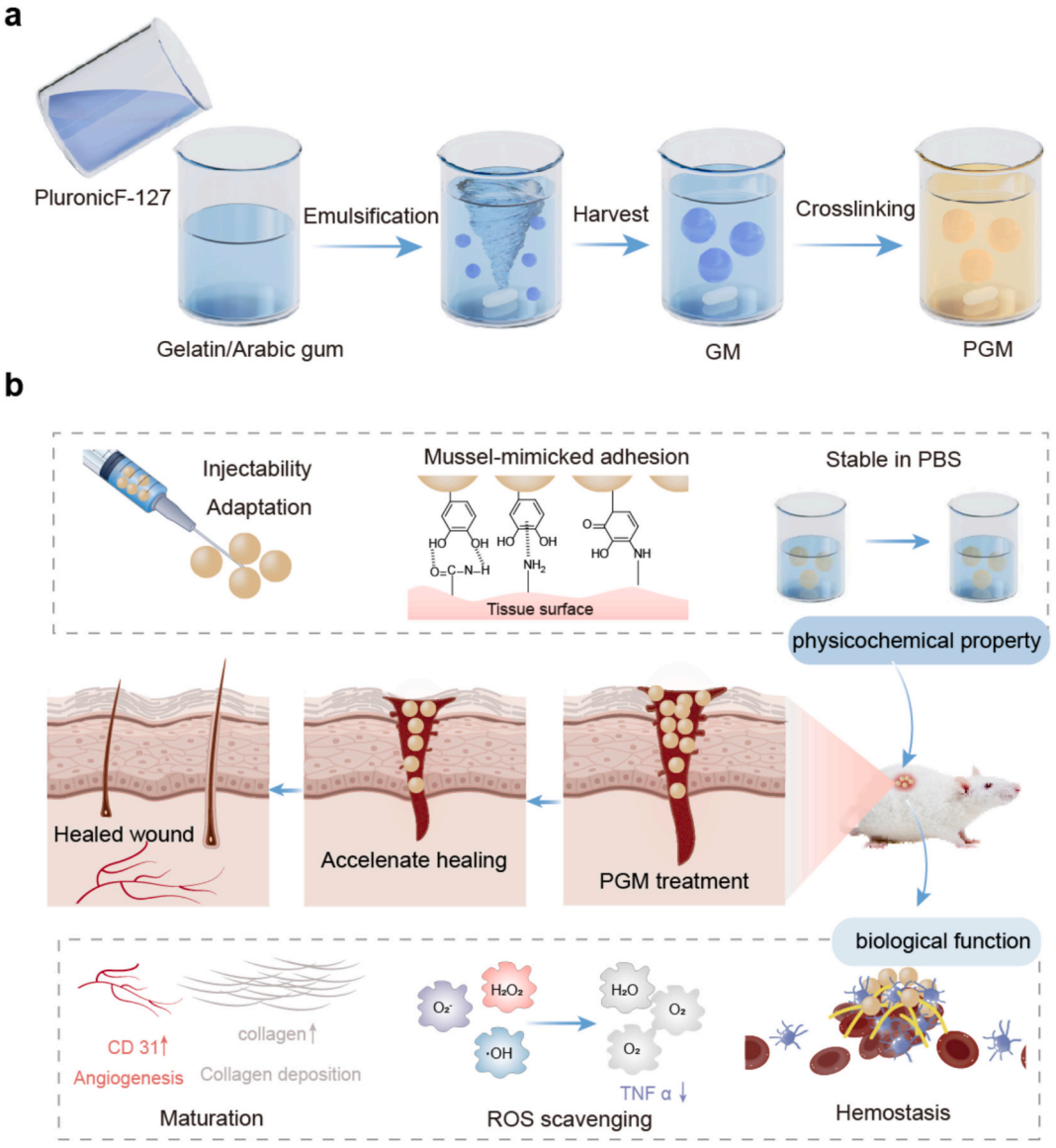

Fig. 1. Schematic depiction of mussel inspired, multifunctional, and drug-free adaptive microgel for accelerating full-thickness wound healing. (a) Techniques for fabrication of PGM. (b) Multifunctional PGM for accelerating wound healing.

as emulsifiers. Then dopamine was oxidized to polydopamine (PDA) and in situ crosslinking GM through a Schiff base or Michael addition reaction [26,27]. By optimizing the water/ethanol volume ratio and surfactant concentration, three sets of microgels with varied sizes were developed. Mussel-inspired PDA used as a crosslinker not only improved microgel stability, but also endowed GM with excellent tissue adhesiveness [28], antioxidative [29,30] and hemostatic activities [31]. In addition, PGM can effectively accelerate full thickness wound healing by promoting hemostasis, exerting anti-inflammatory effects and accelerating collagen deposition and angiogenesis without additional drug agents.

2. Materials and methods

2.1. Materials

Gelatin from porcine skin, Pluronic® F-127 (BioReagent, Mn ~12,600 g/mol), Arabic gum (powder, branched polysaccharide), and dopamine hydrochloride (≥98 %, Mn 189.64) were sourced from Sigma-Aldrich (Shanghai, China). Sodium periodate (ACS reagent, ≥99.8 %, Mn 213.89) and 2,2-Diphenyl-1-picrylhydrazyl (DPPH, Mn 394.32) were purchased from Macklin (Shanghai, China), while the DCFH-DA probe, calcein AM, and propidium iodide were obtained from Solarbio® (Beijing, China).

2.2. Preparation of GM

Gelatin microgels (GMs) were prepared according to a method previously described in the literature [32]. Briefly, 40 mg of gelatin was first dissolved in 10 mL of deionized water at 50 °C, and an amount of ethanol was added, PluronicF127 and Arabic gum were then incorporated into the mixture. For the preparation of small-sized PGM, ethanol was added at a 3:5 volume ratio with water. PF127 and Arabic gum were incorporated at 1:8 and 1:20 mass ratios relative to gelatin, respectively. For medium- and large-sized PGM, the detailed preparation parameters are shown in Table S1. Afterwards, the solution was then stirred at 400 rpm overnight at 25 °C. The solution with microgel was centrifuged at 300*g* for 5 min, then the supernatant removed, and the PGM were purified by washing with PBS and then centrifuged at 1000*g* for 5 min. The washing process was conducted three times to reduce ethanol and surfactant retention. Finally, the sample was resuspended in PBS and stored at 4 °C until use.

2.3. Preparation of PGM

The synthesized GMs were dispersed in a 10 mg/mL of dopamine hydrochloride solution, followed by the addition of $NaIO_4$ at a molar ratio of 0.5:1.0 relative to dopamine. After reacting 3 h at 25 °C, the polydopamine functionalized GMs (PGMs) were gathered by centrifugation at 3000 rpm for 30 min, and washed five times alternately with distilled water to remove pure PDA, and then lyophilized for subsequent experiments [24].

2.4. Characterization

Fourier-transformed infrared spectroscopy (FTIR) spectra of PGM were recorded from 400 to 4000 cm^{-1} using a Bruker Vertex 70 FTIR spectrometer (Germany). ^1H NMR spectroscopy was determined at 600 MHz with a Bruker instrument. D_2O was used to dissolve Pluronic® F-127, Arabic gum and GM. Morphologic images of PGM were obtained under brightfield microscopy (Biotek Cytation 5), and size distributions of PGM were statistically obtained by ImageJ software (NIH, USA). The viscosity curve of the as-prepared PGM was obtained using an Anton Paar Physical MCR 302e rheometer, where shear rate ranged from 0 to 100 1/s. Strain sweep experiments were performed with the amplitude varying from 0.1 % to 100 % strain at 10 rad/s angular frequency.

2.5. Swelling performance of PGM

S-PGM, M-PGM, and L-PGM were soaked in PBS with a pH of 7.4. After 48 h, the weights of the swollen PGM (M2) and the original PGM (M1) were measured. The swelling ratios for S-PGM, M-PGM, and L-PGM were calculated as the ratio of M2 to M1.

2.6. Adhesive performance of PGM

Following well-established method [33], the adhesive strength of PGM to fresh porcine skin was qualitatively determined by a lap-shear test using a universal testing machine (MARK-10, USA). Excess fat was initially trimmed from the porcine skin, and two pieces of pigskin substrate were cut to dimensions of 50 mm in length and 20 mm in width. Subsequently, the PGM was injected into two porcine skin tissue with 20 mm length and 20 mm width. The formed sandwich structure was tested using a universal testing machine with tensile rate of 50 mm/min. Each experiment was performed three times.

2.7. In vitro cytocompatibility of PGM

CCK-8 and live/dead assays were used to analyze the cytocompatibility of L929 cells with PGM. Briefly, the PGM were first soaked in DMEM culture medium for 24 h to obtain 50 mg/mL of dispersion liquid for the follow-up experiment. L929 cells were cultured in DMEM supplemented with 10 % FBS and 1 % penicillin/streptomycin at 37 °C in a humidified 5 % CO_2 atmosphere, and the L929 cells were seeded at 5000 cells per well in a 96-well microplate. After L929 cells adhered to the wall for 12 h, the PGM extraction solution was added. On days 1, 2, and 3, adding 10 μL of CCK-8 solution to each well. After a 3 h incubation period, 100 μL of supernatant was pipetted into 96-well microplate, where its absorbance at 450 nm was then assessed using a multifunctional microplate reader. The following formula was used to determine cytocompatibility:

$$\text{cytocompatibility} = \frac{OD_s - OD_b}{OD_c - OD_b} \times 100\%$$

where OD_s, OD_b and OD_c represent the sample group, blank group, and control group, respectively.

Live/dead staining assay was used to further assess cell viability [34]. L929 cells were seeded at a density of 10,000 cells per confocal dish, and stained cells were examined using confocal laser scanning microscopy (CLSM, Nikon AX, Japan) after 1, 2, and 3 days of culture.

2.8. In vitro hemocompatibility of PGM

The hemolysis assay was performed to evaluate the in vitro hemocompatibility of PGM. To isolate red blood cells (RBCs), 10 mL of anticoagulated rabbit blood was centrifuged at 3000 rpm for 10 min, then discarded the supernatant. The sample was then gently rinsed with PBS and centrifuged at 3000 rpm for 5 min, this process proceeds three times. The RBCs diluted to 10 % (*v*/v) with PBS were then incubated with 1, 2, or 3 mg of PGM. PBS and deionized water were used as a negative control (NC) and positive control (PC), respectively. The samples were incubated for 60 min at 37 °C. The mixture was centrifuged at 2000 rpm for 10 min, after which 100 μL of supernatant was transferred to a 96-well microplate. Absorbance of the supernatant at 540 nm was measured using an enzyme label reader, and hemolysis was determined as follows:

$$\text{hemolysis rate} = \frac{OD_S - OD_{NC}}{OD_{PC} - OD_{NC}} \times 100\%$$

where OD_S, OD_{NC} and OD_{PC} represent the sample, negative control andpositive control group, respectively.

2.9. Cell recruitment and infiltration

L929 cells were seeded in six-well plates at a concentration of 10,000 cells per well, then cultured for 48 h to 80 % confluency. A 200 μL pipette tip was used to scratch the cell monolayer, followed by removing cellular debris. The PGM samples were then introduced into the Transwell chambers and co-cultured with L929 cells, with serum-free medium added as control group. Photomicrographs were captured at 0 and 24 h, representing the initial and subsequent scratch areas. The scratched area was computed by applying Image J software [35], and the percentage scratch area (%) was calculated as follows:

$$\text{percentage scratch area} = \frac{S_t}{S_0} \times 100\%$$

where S_0 and S_t represent initial scratch area and scratch area after 24 h, respectively.

In addition, cell recruitment ability of PGM was evaluated using 24-well Transwell plates (8 μm pores, Corning, USA). L929 cells (10,000 cells per well) were seeded in the upper chambers, S-PGM, M-PGM and L-PGM were placed in the lower chamber. To minimize the effects of cell proliferation, DMEM containing 1 % FBS was added in both upper and lower chamber, respectively. After culturing 24 h, L929 cells in upper chambers were fixed by 4 % paraformaldehyde (PFA) and stained by 0.1 % crystal violet solution (Solaribo, China). After wiping off the non-migrated L929 cells, the migrated L929 cells on the underside of polycarbonate film were observed under a bright field microscope.

2.10. In vitro of cell differentiation

L929 cells were used to evaluate the effect of PGM on differentiation of fibroblasts into myofibroblasts. Added 1 mL of L929 cells at an initial density of 8×10^5 cells per well into a confocal dish and incubate at 37 °C for 12 h to allow for cell adhesion. Then 25 μL of PGM was added in the medium for co-incubation for 48 h, while 25 μL of PBS was added as the control. Subsequently, according to the manufacturer's instructions, added anti- α-SMA antibody and fluorescent antibody, then imaging was performed using CLSM.

2.11. In vitro blood clotting index of PGM

The in vitro blood clotting assay for PGM was conducted in accordance with established methods, involving the application of 20 μL of calcium ion-activated whole blood onto the PGM surface, with Celox hemostatic powder serving as control [16]. Following a 5 min incubation at 37 °C, 5 mL of deionized water was added to dissolve the unstable blood clots, and 100 μL of the supernatant was transferred to a 96-well microplate and absorbance was measured at 540 nm, BCI was determined as follows.

$$\text{BCI} = \frac{OD_s}{OD_c} \times 100\%$$

where OD_s and OD_c represent the sample and control group, respectively.

The stable blood clots were rinsed with PBS and fixed in 4 % *v*/v of PFA for 20 min, followed by dehydration using ethanol at increasing concentrations and freeze-drying. Scanning electron microscopy (SEM, Phenom, Netherlands) was then used to capture images of hemocyte adhesion.

2.12. In vivo hemostatic performance of PGM

The Animal Research Committee of Guizhou Medical University approved all described experimental animal procedures (No.2302043). Hemostasis tests were performed in vivo using the rat-tail amputation model [16]. Female Sprague-Dawley (SD) rats, aged eight weeks, were randomly assigned to four groups. Rats were anesthetized with an intraperitoneal injection of pentobarbital sodium, and following a 2 cm tail incision, 20 mg of Colex or samples were applied to the bleeding site. A pre-weighed filter paper was positioned beneath the tail to measure blood loss, and hemostasis time was recorded. The untreated group served as control group.

2.13. Antioxidant activity of PGM

The DPPH free radical scavenging assay was performed following a method adapted from literature [26]. 25 mg of PGM was added to 2 mL of ethanol solution containing DPPH (100 μM, Macklin, China) and the mixture was then vigorously shaken in the dark. The absorbances of the reaction solutions were then measured at 517 nm after 30 min and 60 min. The remaining DPPH was determined using the following formula:

$$\text{remaining DPPH} = \frac{OD_s}{OD_c} \times 100\%$$

where OD_s and OD_c represent the absorbances of the sample and the ethanol solution, respectively.

The RAW264.7 macrophage cell line was used as our experimental cell line. Cells (8×10 [5]) were seeded in confocal dishes and co-cultured with each sized PGM for 12 h. The cells were rinsed with PBS three times, and then 1 μL of a 10 mM DCFH-DA probe was added to each dish. The mixture was incubated at 37 °C for 20 min. Subsequently, 1 μL of 100 μM H_2O_2 was added, and the mixture was incubated at 37 °C for another 20 min. The culture medium was then discarded, and the cells were rinsed three times with PBS to eliminate the DCFH-DA probe before observation under CLSM [29].

2.14. In vivo wound healing in a full-thickness skin defect model

Six-week-old female SD rats were anesthetized, the dorsal hairs were shaved, and a 10 mm full-thickness wound was created on the mid-back. PGM were applied to wound sites, with an untreated group serving as the control. Wounds were photographed at 0, 3, 7, and 14 days after injury, and the healing rate was determined using Image J software as follows [29]:

$$\text{wound healing rate} = \frac{S_0 - S_t}{S_0} \times 100\%$$

where $S_0$and S_t represent the initial wound area and wound area at each time point post-wounding, respectively.

Tissue regeneration was evaluated through histological and immunohistochemical analyses. Samples were initially fixed in 4 *v*/v% of PFD, then embedded in paraffin wax, and sectioned for H&E as well as Masson trichrome staining, following the manufacturer's guidelines. In addition, immunofluorescence staining with corresponding primary antibodies was performed to assess CD31 and TNF-α levels on day 7 and day 14. Staining samples were deparaffinized, rehydrated, and underwent antigen retrieval. The sections were subsequently blocked with 3 % bovine serum albumin for 30 min and incubated with primary antibodies for 12 h at 4 °C, sections were then incubated with a secondary antibody for 1 h at 25 °C. The sections were ultimately visualized using CLSM, and ImageJ software was utilized to measure the average optical density of each immunohistochemical image.

2.15. Statistical analysis

For this study, experimental data were derived from at least three separate replicates. Analysis and visualization of the data were performed using GraphPad Prism 9.5.0, Image J, and Origin 2021 software. Results are depicted as the mean ± standard deviation, with group comparisons made via one-way ANOVA or *t*-tests. A *p-value of <0.05 was deemed statistically significant.

3. Results and discussion

3.1. Preparation and characterization of PGM

Gelatin microgel (GM) is of significant interest as bioactive matrix due to good biocompatibility, low immunogenicity, and versatile functional groups that can be used for chemical modification [36]. As shown in Fig. 2a, gelatin dissolved in a water-ethanol mixture containing Pluronic F127 and Arabic gum to form a miscible solution under heating and stirring, after cooling the mixture to 25 °C, the gelatin phase separates from ethanol and spherical GM formed because of its reduced solubility in ethanol and thermal gelation in water [24]. Subsequently, the GM dispersed into dopamine solution containing $NaIO_4$ to obtain PDA functionalized gelatin microgel (PGM). Consequently, the developed method enables the controllable and facile generation of PGM, without the need for introducing expensive and complicated microfluidic technology. In addition, Pluronic® F127 and Arabic gum were utilized as surfactants and stabilizers, respectively. There is no problem of biocompatibility issues. Most importantly, the polymerized PDA can endow PGM with excellent tissue adhesion, hemostatic activity, and

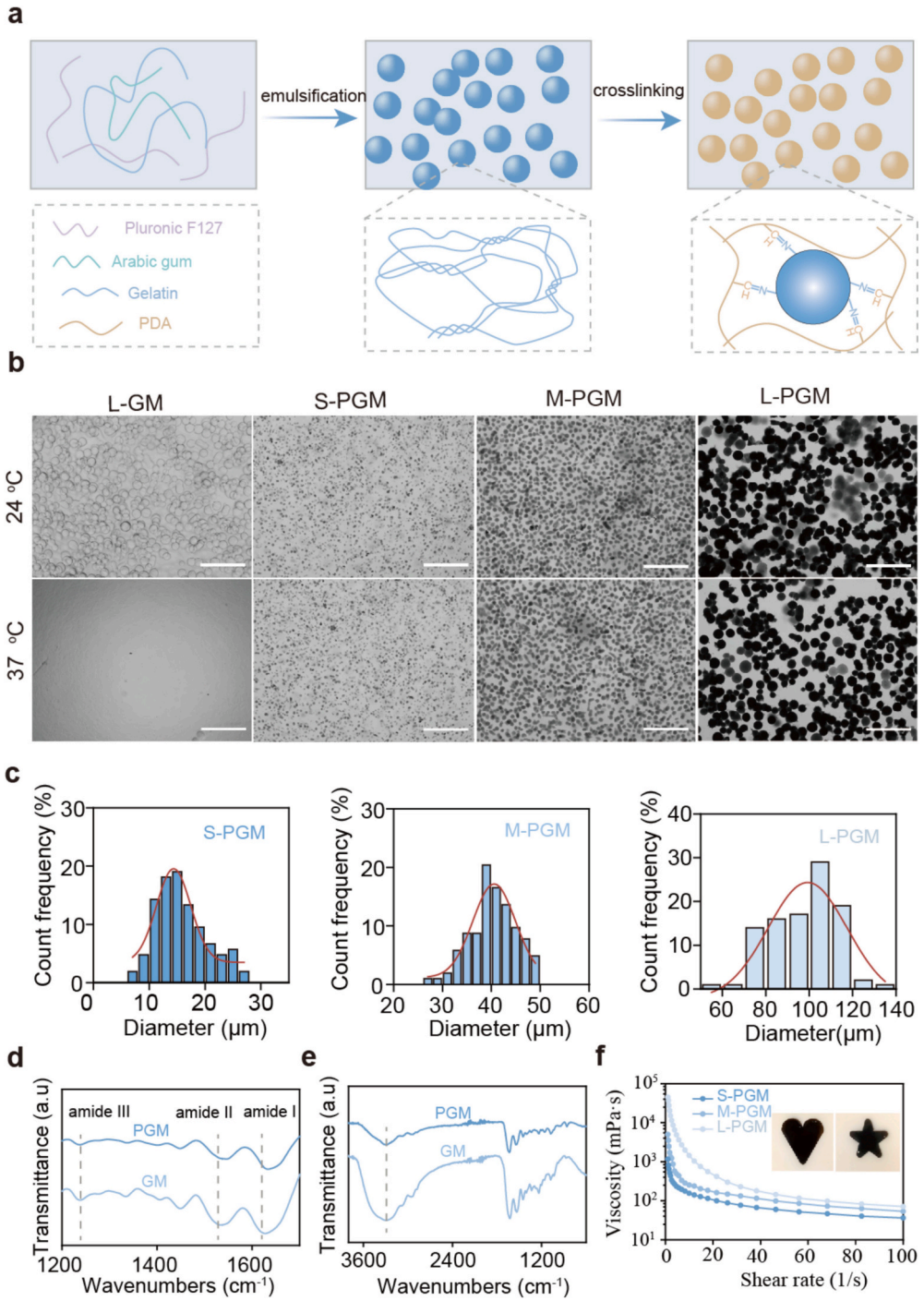

Fig. 2. Preparation and characterization of PGM. (a) Preparation diagram of PGM. (b) Bright-field images of L-GM, S-PGM, M-PGM and L-PGM at 20 °Cand 37 °C, scale bar is 400 μm. (c) Size distribution of S-PGM, M-PGM and L-PGM. (d and e) FTIR spectra of GM and PGM. (f) Viscosity curves for S-PGM, M-PGM, L-PGM and S-PGM in heart, star geometric shapes.

ROS scavenging, making them effective in accelerating full thickness wound healing. Fig. S1 and Fig. S2 illustrate that PDA polymerization caused the appearance of GM to change from transparent to dark brown, indicating that DA oxidation process proceeded, and ^{1}H NMR of Pluronic® F-127, Arabic gum and GM showed that the peaks corresponding to characteristic protons of Pluronic® F-127 did not present in the spectra of GM indicating free of Pluronic® F-127 (Fig. S3). Particularly, crosslinking reaction notably enhanced the stability of GM under physiological condition, Fig. 2b and Fig. S4 revealed that PGM maintained its round shape at both 24 °C and 37 °C. Conversely, GM quickly lost their morphology at 37 °C, suggesting that synchronous crosslinking is in favor of forming a uniform and stable PGM.

In addition, relying on the gelatin phase separates from ethanol originating from reduced solubility in ethanol and thermal gelation in water, spherical GMs with varied size generate via altering ethanol/water volume ratio, and the mass ratios of PF127 and Arabic gum relative to gelatin (Table S1), which preparation parameter can impact gelatin phase separates that is closely associated with solubility, ionic strength, and macromolecular crowding agents [25,37]. Then templated GMs dispersed into dopamine solution containing $NaIO_4$, where dopamine was oxidized by $NaIO_4$, leading to the formation of PDA oligomers, which then reacted with amino groups from GM via Schiff base reactions or Michael addition reactions to obtain PGM. Fig. 2c showed that the controllable sizes of PGM can be achieved through optimizing parameters, PGM with 15 μm, 30 μm and 100 μm in diameters, denoted as S-PGM, M-PGM and L-PGM, respectively, thus proving the possibility of developing PGM with a well-controlled dimensional and distribution range.

The interaction between PDA and gelatin within PGM was investigated using FTIR. Fig. 2d illustrated that the C≐N stretching vibrations of Schiff base group that typically observed at 1600–1650 cm^{-1}, overlapped with the amide I band of gelatin, resulting in a differential peak at 1635 cm^{-1} within PGM. The absorption bands at 3300–3500 cm^{-1}, associated with -OH and -NH_2 stretching, showed a lower frequency in PGM than GM (Fig. 2e), suggesting reduced -NH_2 presence in the PGM and indicating a crosslinking reaction. As shown in Fig. 2f, the viscosity of PGM significantly decreased with an increasing shear rate from 0 to 100 1/s, demonstrating excellent shear-thinning performance. In addition, PGM could be injectable and molded into heart and star shapes, shape adaptability of PGM is conducive to fill gaps and cavities, as well as penetrating deep into ruptured tissue, thereby in-situ sealing to stop bleeding and covering irregular wound [38]. Meanwhile, strain sweep test demonstrated the storage moduli (G') was consistently greater than the loss moduli (G") within linear viscoelastic region, indicating the characteristics of gels (Fig. S5).

3.2. Tissue adhesive performance of PGM

Favorable adaption to wound deformation is crucial for microgels to maintain stability and perform biologic functions during wound repair

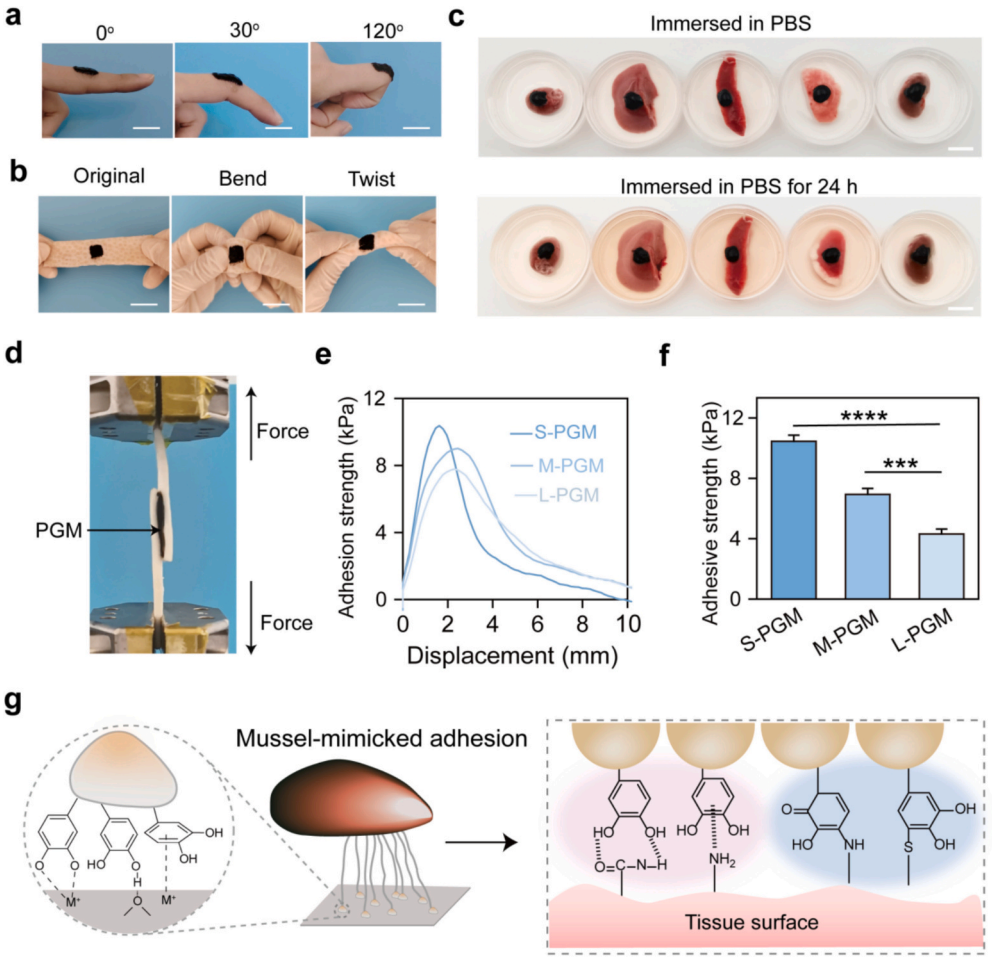

Fig. 3. Tissue adhesive performance of PGM. (a) Photographs of S-PGM adhering to the finger with 0°, 30° and 120°, scale bar is 2 cm. (b) Photographs of S-PGM adhering to porcine skin following bending, twisting, scale bar is 2 cm. (c) Photographs of S-PGM adhering to heart, liver, spleen, lung and kidney surface and after in PBS at room temperature for 24 h, scale bar is 1 cm. (d) Photograph of the lap shear test. (e) Representative force-displacement curves of S-PGM, M-PGM and L-PGM adhering to porcine skin. (f) Adhesive strength of f S-PGM, M-PGM and L-PGM adhering to porcine skin. (g) Mussel inspired tissue-adhesive mechanism for PGM. Statistical significance: ***$p < 0.001$, ****$p < 0.0001$.

[39,40]. Mussels exhibit strong adhesion to diverse biological surfaces, primarily due to the presence of 3,4-dihydroxy-*L*-phenylalanine. Dopamine (DA) and polydopamine (PDA), as derivatives of this compound, share similar adhesive performance [27]. Fig. 3a shows that this mussel-inspired bio-adhesive performance makes PGM effective, long-lasting, and practical wound dressing, even for finger joints. The PGM demonstrated adaptability to complex deformation, maintaining stable adhesion to porcine skin despite significant bending or twisting (Fig. 3b). Particularly, PGM displayed excellent adhesion to various organs at 37 °C, such as heart, liver, spleen, lung and kidney, and can maintain stable adhesion even when immersed in PBS after 24 h (Fig. 3c), and no obvious changes for PGMs swelling ratio at 37 °C were observed in PBS for 48 h (Fig. S6), indicating excellent stability of PGM. In addition, 4 °C storage conditions for 2 weeks also showed excellent stability (Fig. S7). Subsequently, lap shear tests using porcine skin as a biologic tissue model were conducted to quantitatively assess the adhesive performance of PGM (Fig. 3d). As shown in Fig. 3e and f, the adhesive strengths of S-PGM, M-PGM, and L-PGM adhering to porcine skin were 10.3 kPa, 8.9 kPa, and 7.6 kPa, respectively. S-PGM displayed the highest adhesive strength, this is because of the increase in specific surface area, leading to higher density of catechol groups [41,42]. As shown in Fig. 3g, recent studies have demonstrated that catechol groups within PDA play an essential role in mussel-mimicked adhesion, the interactions of PGM with tissue surface mainly comes down to non-covalent bonding and covalent bonding [42]. Catechol groups within PGM bind to tissue through coordination bond and hydrogen bond. Moreover, the catechol group, known for its high binding affinity, can bond with other nucleophiles such as thiol and imidazole present on the tissue surface via Schiff base reactions and/or Michael addition [43]. Altogether, the mussel-inspired bio-adhesive property makes PGM attach to tissue surfaces even in wet microenvironment, thus assisting integration to host tissue.

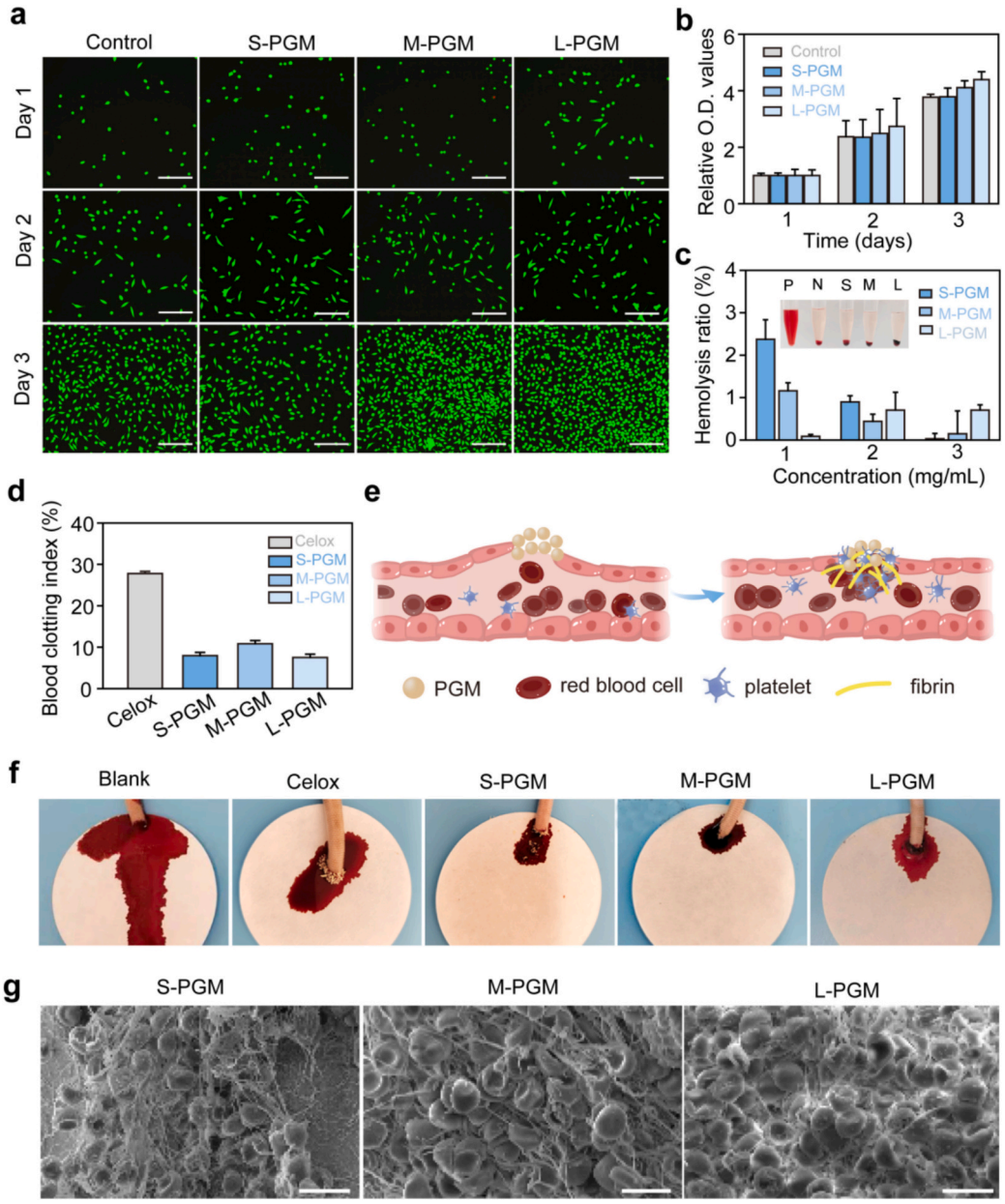

Fig. 4. Biocompatibility and hemostatic performance of PGM. (a) Confocal images of L929 cells co-cultured with PGM, scale bar is 200 μm. (b) Proliferation of L929 cells co-cultured with PGM. (c) Hemolysis rate of PGM. (d) In vitro blood clotting index of PGM. (e) The potential hemostatic mechanism of PGM. (f) Representative photographs of bleeding 1 min after treatment with PGM. (g) SEM images of hemocyte adhesion on PGM, scale bar is 8 μm. Statistical significance: $^{***}p < 0.001$.

3.3. Biocompatibility and hemostatic performance of PGM

Favorable cytocompatibility is a critical factor in determining the biomedical applications of PGM. Live/dead staining first performed to evaluate the cytocompatibility of PGM. Fig. 4a showed that the majority of spindle-shaped L929 cells stained green that indicates living cell, while few L929 cells stained red that indicates dead cell. Then cytocompatibility quantitatively assessed using Cell Counting Kit-8 (CCK-8) assay, as shown in Fig. 4b, the proliferative trend for L929 cells in the PGM group was equivalent to that of control group over three days. Both of which confirmed that the developed PGM displayed favorable cytocompatibility in vitro. In addition, cell migration assay performed to determine the influence of PGM on cell migration. Scratch assays on L929 cells were used to evaluate cell migratory rates in co-culture with the PGM, and Fig. S8 reveals that the migration rates of L929 cells in control group, S-PGM group, M-PGM group, and L-PGM group were 21.3 %, 84.3 %, 64.8 %, and 55.0 %, respectively (Fig. S9). Previous studies have shown that gelatin and PDA promote cell adhesion and proliferation, thereby facilitating scratch wound healing [44,45]. The potential of PGM recruiting endogenous fibrocytes was also performed in vitro by using Transwell apparatus. S-PGM, M-PGM and L-PGM were put in the lower chambers while L929 cells were seeded on the upper chambers. It was found that the number of migrated cells in PGM is significantly higher than that in the control group (Fig. S10). These outcomes suggest that PGM has the potential to promote the recruitment and migration of endogenous fibrocytes. In addition, we used immunofluorescence to analyze the effects of PGM on the differentiation of fibroblasts into the highly contractile α-SMA-positive myofibroblasts. It was found that L929 cells co-culturing with PGM significantly inhibited the differentiation into myofibroblasts (Fig. S11), indicating that PGM shows a pronounced anti-fibrotic effect.

In addition to cytocompatibility, hemocompatibility is another non-negligible concern for wound dressings. The hemolysis ratio of diluted RBCs in direct contact with PGM was determined to evaluate hemocompatibility (Fig. 4c). The vivid red color of supernatants in deionized water group (positive control) signified hemoglobin leakage originating from damaged red blood cells, while the supernatant for all PGM groups exhibited light-yellow color, which is consistent with PBS group (negative control). The hemolysis ratio for all PGM groups was quantified to be under 3 %, remaining below the acceptable threshold of 5 % [46].

Bleeding is common during trauma first-aid and surgical debridement, and microgel dressings with hemostatic activity is fundamental to wound healing process [47]. The hemostatic efficacy of PGM was assessed in vitro through a whole-blood clotting assay. 20 μL of recalcified whole blood was added into 5 mg of PGM sample and incubated the mixture at 37 °C for 5 min. The uncoagulated blood then washed by adding 5 mL of deionized water. A red supernatant signified limited coagulation, while a lower blood-clotting index (BCI) reflected superior hemostatic activity. Fig. S12 reveals that the supernatant in PGM groups exhibited minimal redness, indicating superior blood coagulation capacity. The hemoglobin content in supernatant then quantified by measuring absorbance at 540 nm, and Fig. 4d indicated that the BCI for S-PGM, M-PGM, and L-PGM were 7.9 %, 10.8 % and 7.5 %, respectively, which were lower than the commercialized Celox hemostatic powder group (27.8 %). As shown in Fig. 4e, the superior blood clotting performance of PGM was primarily due to the fact that PDA could induce platelet adhesion and enhance erythrocyte aggregation, thus activating the exogenous coagulation system for rapid blood clotting [31]. The hemostatic capacity of PGM was evaluated by creating a rat-tail amputation model, and Fig. 4f demonstrated that the PGM groups exhibited significantly smaller bleeding regions than both the control and Colex groups. Quantitative hemostatic capacity was evaluated by determining blood loss within 1 min, and Fig. S13 showed that the control and Colex groups displayed 517 mg and 238 mg of blood losses, respectively, whereas the S-PGM, M-PGM, and L-PGM groups demonstrated significantly reduced blood losses of 105 mg, 80 mg, and 137 mg. The different hemostatic performance of the S-PGM, M-PGM, and L-PGM groups may be attributed to the fact that reducing the PGM size is in favor of the formation of larger specific surface area. Thus, the PGM exhibited a desirable hemostatic effect, which was in favor of follow-up wound healing. In addition, SEM was used to analyze the adhesion and spreading morphologies of RBCs on PGM surface, and Fig. 4g demonstrates that numerous normally shaped RBCs adhered to the PGM surface, suggesting that the PGM effectively captured and activated RBCs.

3.4. Antioxidant activity of PGM

Reactive oxygen species (ROS) generating at wound sites can destruct cellular proteins, lipids, and DNA, potentially hindering the healing process [48]. It is well known that that PDA exhibits excellent radical scavenging and multi-antioxidative capacity through preventing the production of free radicals or/and direct interaction with free radicals [41]. In this work, the antioxidant activity of PGM was initially evaluated using DPPH radical scavenging assay, as the catechol groups in polydopamine can neutralize the stable free radical molecule DPPH [26]. PGM with varied sizes were in contact with DPPH solution and reacted in darkness for 30 and 60 min to determine DPPH-scavenging efficiency. Fig. 5a depicted a notable color change from deep purple to yellow, signifying strong antioxidant activity. Then antioxidant activity of PGM was determined with diminished absorbance of DPPH at 517 nm (Fig. 5b). In particular, the antioxidant activity of PGM exhibited size dependence, with the DPPH-scavenging efficiency of L-PGM group at approximately 75 % at 60 min, inferior to the S-PGM and M-PGM groups that were both near 87 % at 60 min. This was likely because of an increase in the specific surface area, leading to higher density of catechol groups, thus improving the antioxidant efficiency [41]. In addition, PGMs were co-cultured with H_2O_2-induced macrophages to assess the in vitro ROS scavenging capabilities. DCFH-DA probe was used to label intracellular ROS levels in each group to assess antioxidant capacity via CLSM observation, significant elevation in levels in the H_2O_2 group was found, whereas co-culturing with PGM notably reduced these levels, with S-PGM exhibiting the lowest intracellular ROS levels (Fig. 5c), suggesting that PGMs can reduce intracellular oxidative stress, preserving the redox balance within the cells. As shown in Fig. 5d, the 1,2-dihydroxybenzene structure within PGM can oxidize into quinones to donate either a single electron or hydrogen atom, which possess robust ability to capture ROS, thus realizing an efficient antioxidant capacity. In addition, reducing the PGM size could increase the antioxidant capacity, this is because of the formation of larger specific surface area.

3.5. In vivo wound healing in a full-thickness skin defect model

The potential of utilizing PGMs as wound dressing was further evaluated, a 10-mm diameter circular defect on dorsum of rats was developed and representative wound closures over the following 14 days were photographed (Fig. 6a and b). The wound areas exhibited wound healing with a gradual diminution in size and it was found that the wounds treated with PGM groups were superior to control and GelMA group, displaying a significant efficacy in promoting wound closure. Quantitative analyses of wound areas surrounding wound closure are presented in Fig. 6c. On day 7, the wound contraction ratios in L-PGM, M-PGM, and S-PGM groups were 80.6 %, 79.3 %, and 85.6 %, respectively, which were significantly higher than in the control group (60.5 %) and GelMA group (67 %). By day 14, the scab had completely detached, and the wounds had nearly fully healed in all PGM groups, in contrast to the control group, where 7.1 % still exhibited non-healed wounds. These results indicated that PGMs exhibited a better wound-healing effect, which was mainly attributed to the fact that PGM can accelerate cell migration and ECM remodeling, thus contributing to tissue regeneration.

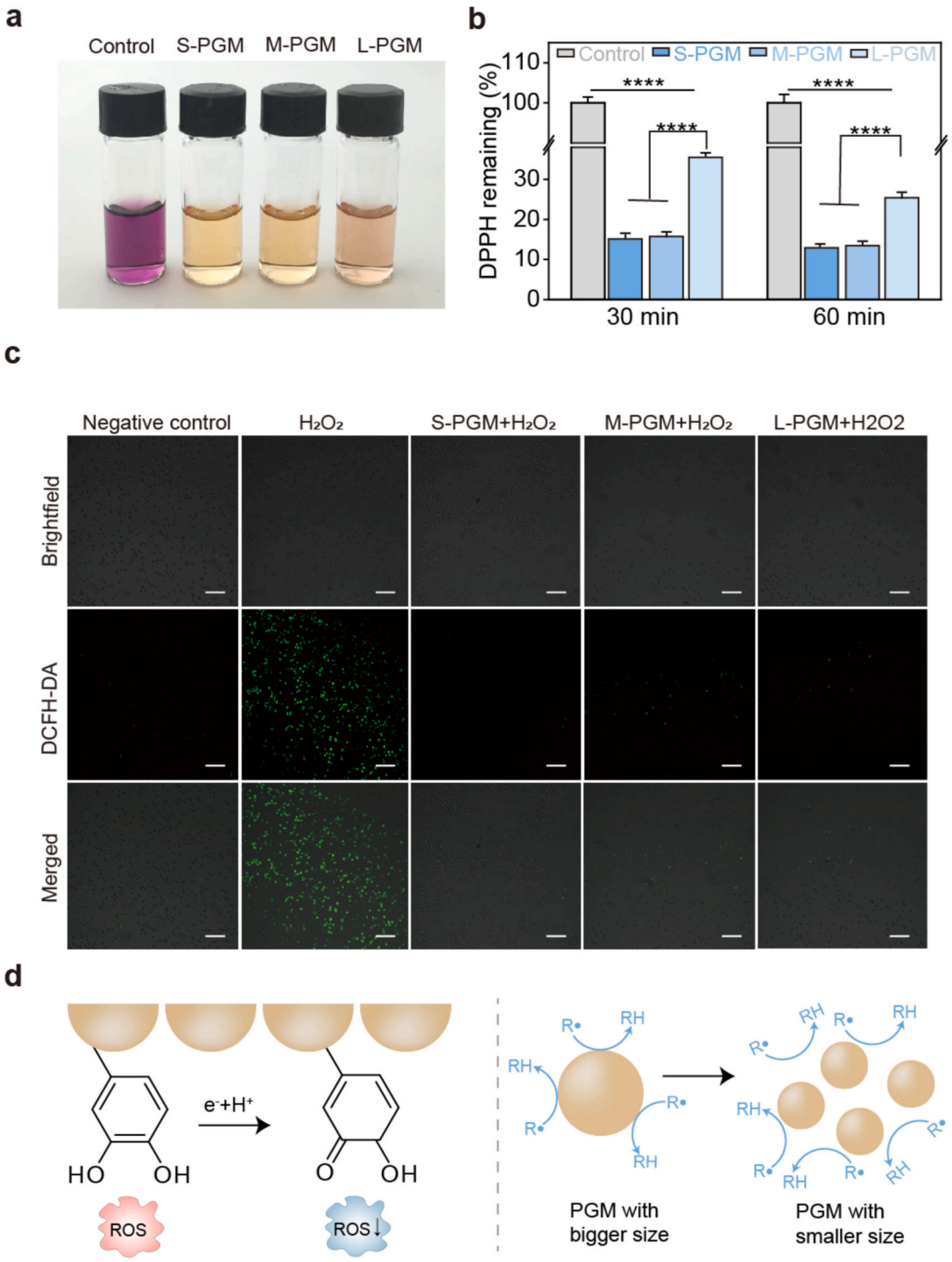

Fig. 5. Antioxidant performance of PGM. (a) Images of DPPH scavenging ability over 30 min for all groups. (b) DPPH scavenging abilities for S-PGM, M-PGM, and L-PGM. (c) Intracellular ROS-scavenging performance of macrophages co-cultured with PGM, scale bar is 200 μm. (d) Radical scavenging mechanism and the size-tuning strategy for regulating radical scavenging ability of PGM. Statistical significance: ****$p < 0.0001$.

To assess the impact of PGM on wound healing, H&E, Masson's trichrome, and Sirius red staining were performed to evaluate the skin regeneration and collagen deposition. Fig. S14 and Fig. S15 showed that PGM can effectively promote wound closure. As shown in Fig. 6d, H&E staining of day 14 showed that all three PGM groups displayed obvious re-epithelialization, granulation tissue and new skin attachment formation, while the control group exhibited residual scabs, indicating the superior healing efficiency of PGM. To quantify the morphological changes occurring in progression of healing, Image J was used to determine the wound area length. Fig. S16 revealed that the PGM group displayed smaller wound length. Furthermore, the regenerated skin in all PGM groups displayed a more organized structure, a greater number of regenerated cutaneous appendages were observed, such as hair follicles and sweat glands. Collagen deposition is a key process in skin wound remodeling and serves as a benchmark for assessing wound healing [29]. Collagen deposition in the wound area was further evaluated by using Masson's trichrome and Sirius red staining, and it was found that PGM-treated wounds healed with a remarkably higher degree

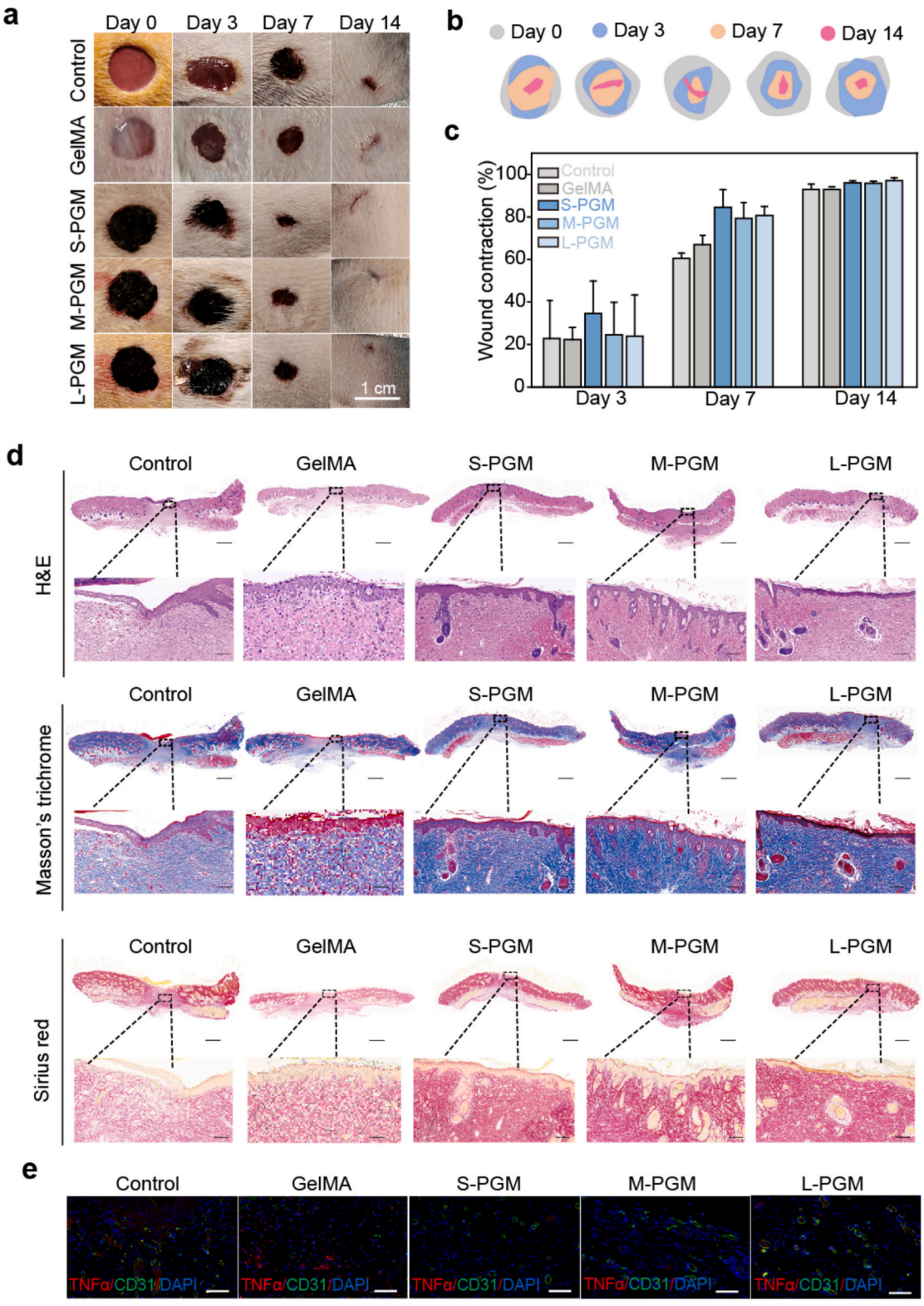

Fig. 6. In vivo full-thickness skin wound repair in rat models. (a) Representative macroscopic images and (b) superimposed images of wound closure with GelMA, S-PGM, M-PGM, and L-PGM treatments on days 0, 3, 7, and 14. (c) Percentage area of wound closure during 14-day healing. (d) H&E staining, Masson's staining, and Sirius red staining of the regenerated wound sections, scale bar is 50 μm. (e) Images of immunofluorescence staining of TNF-α and CD31 in tissue sections, scale bar is 100 μm.

of collagen deposition and a more organized fibrous structure than in control group, and corresponding quantitative analysis showed that the collagen deposition rate was about 60 % in PGM, which was higher than in control and GelMA group (Fig. S17), implying that PGM improve collagen deposition, facilitating skin reconstruction. Sirius red staining results indicated that PGM significantly enhanced type I collagen production in wound tissue by day 14.

In addition, immunostaining analysis showed significantly less TNF-

α expression and higher CD31 expression in PGM group relative to control group, indicating that PGM suppressed the inflammatory response and promoted new blood vessel formation (Fig. 6e, S18-S19). These results demonstrated the superior efficacy of PGMs in repairing full-thickness skin defects on basis of the combined effect of their inherent antioxidant activity, suppressed inflammation, enhanced angiogenesis and collagen deposition.

4. Conclusion

A multifunctional microgel dressing was developed through cross-linking sacrificial gelatin microgels with a modified emulsification-chemical crosslinking technique. The as-prepared PGM showed excellent stability, tissue adhesion, hemostatic activity, ROS scavenging capability, and wound sealing due to in situ polydopamine formation. PGM exhibited outstanding hemostatic activity, as evidenced by whole blood coagulation both in vitro and in vivo adopting the mouse tail amputation model. In addition, PGM exhibited effective antioxidant activity, enhancing the microenvironment to support cell growth and biologic functions under oxidative conditions. PGM also effectively promoted wound healing by facilitating angiogenesis and collagen regeneration, decreasing the secretion of TNF-α. Due to its rapid and effective hemostatic capability, adaptability to irregular surfaces, and exceptional antioxidative and wound healing performance, PGM shows potential as a versatile wound dressing suitable for various applications. However, further optimization and exploration are needed for evaluating the biocompatibility, production cost, and quality control of PGMs in specific clinical translation. Typically, integrating a variety of disciplines, including chemistry, materials science, and regenerative medicine may be an effective strategy.

CRediT authorship contribution statement

Lijing Teng: Writing – review & editing, Writing – original draft, Methodology, Investigation, Data curation. **Honghong Zhang:** Writing – review & editing, Writing – original draft, Methodology, Data curation. **Xiaomin Sun:** Writing – review & editing, Writing – original draft, Methodology. **Xinping Wang:** Data curation, Formal analysis, Methodology, Writing – review & editing. **Yeshuang Zhong:** Writing – review & editing, Software, Formal analysis. **Simian Zhu:** Writing – review & editing, Software, Methodology, Data curation. **Xiangyu Zeng:** Writing – review & editing, Software, Formal analysis. **Yu Dong:** Writing – review & editing, Software, Formal analysis. **Zhu Zeng:** Writing – review & editing, Supervision, Resources, Funding acquisition. **Zhou Li:** Writing – review & editing, Supervision, Methodology. **Qiang Zheng:** Writing – review & editing, Writing – original draft, Supervision, Methodology.

Declaration of competing interest

The authors declare no competing interests.

Acknowledgements

This study was supported by the National Natural Science Foundation of China grants (32360235 to L.T., 62461009 to Q.Z., 32371373, 12132006 to Z.Z., 32460235 to X.S), the Guizhou Provincial Key Technology R&D Program (2024161 to Q.Z.), the Guizhou Provincial Basic Research Program (Natural Science) (ZK[2022]-381 to L.T.; ZK [2023]032 to Q.Z.; ZK[2024]135 to X.S), the Science and Technology Fund of Guizhou Provincial Health Commission (gzwkj2024-188 to X.S); the Engineering center of Guizhou medical university ([2024]002 to Q. Z.), the Local Science Foundation of Guizhou Province Guided by the Central Committee of China ([2025]024 to Z.Z.), the Guizhou Key Laboratory of Microbio and Infectious Disease Prevention & Control (ZDSYS[2023]004 to Z.Z.), the Youth Science and Technology Talent Development Project of Guizhou Medical University (22QNRC01 to L. T.).

Appendix A. Supplementary data

Supplementary data to this article can be found online at https://doi.org/10.1016/j.ijbiomac.2025.143997.

Data availability

Data will be made available on request.

References

[1] C. Wang, E. Shirzaei Sani, C.-D. Shih, C.T. Lim, J. Wang, D.G. Armstrong, W. Gao, Wound management materials and technologies from bench to bedside and beyond, Nat. Rev. Mater. (2024) 1–17.
[2] Y. Liang, J. He, B. Guo, Functional hydrogels as wound dressing to enhance wound healing, ACS Nano 15 (8) (2021) 12687–12722.
[3] J. Jin, C. Sun, K. Xu, X. Sun, L. Cao, L. Liu, Multifunctional self-healing peptide hydrogel for wound healing, Int. J. Biol. Macromol. 261 (2024) 129734.
[4] Y.J. Fu, R.K. Wang, C.Y. Ma, L.Y. Wang, S.Y. Long, K. Li, X. Zhao, W. Yang, Injectable oxygen-carrying microsphere hydrogel for dynamic regulation of redox microenvironment of wounds, Small 2403781 (2024).
[5] P.-F. Cai, B.-D. Zheng, Y.-L. Xu, B.-X. Li, Z.-Y. Liu, Y.-Y. Huang, J. Ye, M.-T. Xiao, Multifunctional fish-skin collagen-based hydrogel sealant with dual-dynamic-bond cross-linked for rapid hemostasis and accelerated wound healing, Int. J. Biol. Macromol. 266 (2024) 131179.
[6] B.-D. Zheng, L. Gan, L.-Y. Tian, G.-H. Chen, Protein/polysaccharide-based hydrogels loaded probiotic-mediated therapeutic systems: a review, Int. J. Biol. Macromol. 253 (2023) 126841.
[7] C. Ouyang, H. Yu, L. Wang, Z. Ni, X. Liu, D. Shen, J. Yang, K. Shi, H. Wang, Tough adhesion enhancing strategies for injectable hydrogel adhesives in biomedical applications, Adv. Colloid Interf. Sci. 102982 (2023).
[8] B.-D. Zheng, J. Ye, Y.-C. Yang, Y.-Y. Huang, M.-T. Xiao, Self-healing polysaccharide-based injectable hydrogels with antibacterial activity for wound healing, Carbohydr. Polym. 275 (2022) 118770.
[9] B.-D. Zheng, M.-T. Xiao, Polysaccharide-based hydrogel with photothermal effect for accelerating wound healing, Carbohydr. Polym. 299 (2023) 120228.
[10] E. Hasanzadeh, A. Seifalian, A. Mellati, J. Saremi, S. Asadpour, S.E. Enderami, H. Nekounam, N. Mahmoodi, Injectable hydrogels in central nervous system: unique and novel platforms for promoting extracellular matrix remodeling and tissue engineering, Mater. Today Bio 20 (2023) 100614.
[11] M.J. Khiabani, S. Soroushzadeh, A. Talebi, A. Samanta, Shear-induced cycloreversion leading to shear-thinning and autonomous self-healing in an injectable, shape-holding collagen hydrogel, ACS Appl. Mater. Interfaces 16 (41) (2024) 55056.
[12] R.S. Hsu, P.Y. Chen, J.H. Fang, Y.Y. Chen, C.W. Chang, Y.J. Lu, S.H. Hu, Adaptable microporous hydrogels of propagating NGF-gradient by injectable building blocks for accelerated axonal outgrowth, Adv. Sci. 6 (16) (2019) 1900520.
[13] Q. Feng, D. Li, Q. Li, X. Cao, H. Dong, Microgel assembly: fabrication, characteristics and application in tissue engineering and regenerative medicine, Bioact. Mater. 9 (2022) 105–119.
[14] Q. Feng, Q. Li, H. Wen, J. Chen, M. Liang, H. Huang, D. Lan, H. Dong, X. Cao, Injection and self-assembly of bioinspired stem cell-laden gelatin/hyaluronic acid hybrid microgels promote cartilage repair in vivo, Adv. Funct. Mater. 29 (50) (2019) 1906690.
[15] Q. Feng, H. Gao, H. Wen, H. Huang, Q. Li, M. Liang, Y. Liu, H. Dong, X. Cao, Engineering the cellular mechanical microenvironment to regulate stem cell chondrogenesis: insights from a microgel model, Acta Biomater. 113 (2020) 393–406.
[16] B. Li, H. Li, H. Chen, Y. Liu, J. Chen, Q. Feng, X. Cao, H. Dong, Microgel assembly powder improves acute hemostasis, antibacterial, and wound healing via in situ co-assembly of erythrocyte and microgel, Adv. Funct. Mater. 33 (36) (2023) 2302793.
[17] Y.J. Fu, R.K. Wang, C.Y. Ma, L.Y. Wang, S.Y. Long, K. Li, X. Zhao, W. Yang, Injectable oxygen-carrying microsphere hydrogel for dynamic regulation of redox microenvironment of wounds, Small 20 (42) (2024) 2403781.
[18] Q. Xie, C. Yan, G. Liu, L. Bian, K. Zhang, In situ triggered self-contraction bioactive microgel assembly accelerates diabetic skin wound healing by activating mechanotransduction and biochemical pathway, Adv. Mater. 36 (38) (2024) 2406434.
[19] Y. Han, J. Yang, W. Zhao, H. Wang, Y. Sun, Y. Chen, J. Luo, L. Deng, X. Xu, W. Cui, Biomimetic injectable hydrogel microspheres with enhanced lubrication and controllable drug release for the treatment of osteoarthritis, Bioact. Mater. 6 (10) (2021) 3596–3607.
[20] N.D. Caprio, M.D. Davidson, A.C. Daly, J.A. Burdick, Injectable MSC spheroid and microgel granular composites for engineering tissue, Adv. Mater. 36 (14) (2024) 2312226.
[21] J. Wu, G. Li, T. Ye, G. Lu, R. Li, L. Deng, L. Wang, M. Cai, W. Cui, Stem cell-laden injectable hydrogel microspheres for cancellous bone regeneration, Chem. Eng. J. 393 (2020) 124715.

[22] L. Xuan, Y. Hou, L. Liang, J. Wu, K. Fan, L. Lian, J. Qiu, Y. Miao, H. Ravanbakhsh, M. Xu, Microgels for cell delivery in tissue engineering and regenerative medicine, Nano-Micro Lett. 16 (1) (2024) 218.
[23] Y. Shen, Y. Xu, Z. Yu, G. Chen, B. Chen, L. Liao, Multifunctional injectable microspheres containing "naturally-derived" photothermal transducer for synergistic physical and chemical treating of acute osteomyelitis through sequential immunomodulation, ACS Nano 18 (7) (2024) 5483–5497.
[24] L. Ouyang, J.P. Wojciechowski, J. Tang, Y. Guo, M.M. Stevens, Tunable microgel-templated porogel (MTP) bioink for 3D bioprinting applications, Adv. Healthc. Mater. 11 (8) (2022) 2200027.
[25] A.J. Seymour, S. Shin, S.C. Heilshorn, 3D printing of microgel scaffolds with tunable void fraction to promote cell infiltration, Adv. Healthc. Mater. 10 (18) (2021) 2100644.
[26] J. Chen, X. An, L. Xu, Y. Gao, M. Zhou, Z. Liu, Adhesive nanoparticle-in-microgel system with ROS scavenging capability and hemostatic activity for postoperative adhesion prevention, Small 2306598 (2024).
[27] K. Chen, F. Wang, R. Ding, Z. Cai, T. Zou, A. Zhang, D. Guo, B. Ye, W. Cui, M. Xiang, Adhesive and injectable hydrogel microspheres for inner ear treatment, Small 18 (36) (2022) 2106591.
[28] M. Suneetha, S. Zo, S.M. Choi, S.S. Han, Antibacterial, biocompatible, hemostatic, and tissue adhesive hydrogels based on fungal-derived carboxymethyl chitosan-reduced graphene oxide-polydopamine for wound healing applications, Int. J. Biol. Macromol. 241 (2023) 124641.
[29] Y. Wang, Y. Zhang, Y.-P. Yang, M.-Y. Jin, S. Huang, Z.-M. Zhuang, T. Zhang, L.-L. Cao, X.-Y. Lin, J. Chen, Versatile dopamine-functionalized hyaluronic acid-recombinant human collagen hydrogel promoting diabetic wound healing via inflammation control and vascularization tissue regeneration, Bioact. Mater. 35 (2024) 330–345.
[30] Q. Han, L. Bai, Y. Qian, X. Zhang, J. Wang, J. Zhou, W. Cui, Y. Hao, X. Yang, Antioxidant and anti-inflammatory injectable hydrogel microspheres for in situ treatment of tendinopathy, Regener, Biomater 11 (2024) rbae007.
[31] J. Hwang, P. Im, M.K. Kim, J. Kim, Polydopamine-coated silk fiber with controllable length for enhanced hemostatic application, Biomacromolecules 25 (4) (2024) 2597–2606.
[32] A. Lee, A. Hudson, D. Shiwarski, J. Tashman, T. Hinton, S. Yerneni, J. Bliley, P. Campbell, A. Feinberg, 3D bioprinting of collagen to rebuild components of the human heart, Science 365 (6452) (2019) 482–487.
[33] F. Gao, X. Ma, F. Wang, F. Zhou, J. Ye, D. Yang, M. Li, P. Wang, Injectable multifunctional DNA hydrogel for accelerated wound healing, Chem. Eng. J. 470 (2023) 144347.
[34] X. Zhao, S. Li, X. Du, W. Li, Q. Wang, D. He, J. Yuan, Natural polymer-derived photocurable bioadhesive hydrogels for sutureless keratoplasty, Bioact. Mater. 8 (2022) 196–209.
[35] H. Xie, Z. Wang, R. Wang, Q. Chen, A. Yu, A. Lu, Self-healing, injectable hydrogel dressing for monitoring and therapy of diabetic wound, Adv. Funct. Mater. 2401209 (2024).
[36] J.I. Kang, K.M. Park, Advances in gelatin-based hydrogels for wound management, J. Mater. Chem. B 9 (6) (2021) 1503–1520.
[37] Y. Xu, R. Qi, H. Zhu, B. Li, Y. Shen, G. Krainer, D. Klenerman, T.P. Knowles, Liquid–liquid phase-separated systems from reversible Gel–Sol transition of protein microgels, Adv. Mater. 33 (33) (2021) 2008670.
[38] W. Li, Y. Zheng, W. Pang, P. Lai, Bio-inspired adhesive hydrogel for wound healing, Biomed. Tech. 1 (2023) 65–72.
[39] Y. Wang, C. Zhou, Z. Li, G. Li, Y. Zou, X. Li, P. Gu, J. Liu, L. Bai, H. Yan, Injectable immunoregulatory hydrogels sequentially drive phenotypic polarization of macrophages for infected wound healing, Bioact. Mater. 41 (2024) 193–206.
[40] H. Ren, Z. Zhang, X. Cheng, Z. Zou, X. Chen, C. He, Injectable, self-healing hydrogel adhesives with firm tissue adhesion and on-demand biodegradation for sutureless wound closure, Sci. Adv. 9 (33) (2023) eadh4327.
[41] J. Hu, L. Yang, P. Yang, S. Jiang, X. Liu, Y. Li, Polydopamine free radical scavengers, Biomater. Sci. 8 (18) (2020) 4940–4950.
[42] Y. Xu, J. Hu, J. Hu, Y. Cheng, X. Chen, Z. Gu, Y. Li, Bioinspired polydopamine hydrogels: strategies and applications, Prog. Polym. Sci. 101740 (2023).
[43] F. Zhou, Y. Yang, W. Zhang, S. Liu, A.B. Shaikh, L. Yang, Y. Lai, H. Ouyang, W. Zhu, Bioinspired, injectable, tissue-adhesive and antibacterial hydrogel for multiple tissue regeneration by minimally invasive therapy, Appl. Mater. Today 26 (2022) 101290.
[44] V. Alinezhad, K. Esmaeilzadeh, H. Bagheri, H. Zeighami, A. Kalantari-Hesari, R. Jafari, P. Makvandi, Y. Xu, H. Mohammadi, M.-A. Shahbazi, Engineering a platelet-rich plasma-based multifunctional injectable hydrogel with photothermal, antibacterial, and antioxidant properties for skin regeneration, Biomater. Sci. 11 (17) (2023) 5872–5892.
[45] T. Liu, Z. Feng, Z. Li, Z. Lin, L. Chen, B. Li, Z. Chen, Z. Wu, J. Zeng, J. Zhang, Carboxymethyl chitosan/sodium alginate hydrogels with polydopamine coatings as promising dressings for eliminating biofilm and multidrug-resistant bacteria induced wound healing, Int. J. Biol. Macromol. 225 (2023) 923–937.
[46] R. Haghniaz, H. Montazerian, A. Rabbani, A. Baidya, B. Usui, Y. Zhu, M. Tavafoghi, F. Wahid, H.J. Kim, A. Sheikhi, Injectable, antibacterial, and hemostatic tissue sealant hydrogels, Adv. Healthc. Mater. 12 (31) (2023) 2301551.
[47] J. Cheng, H. Wang, J. Gao, X. Liu, M. Li, D. Wu, J. Liu, X. Wang, Z. Wang, P. Tang, First-aid hydrogel wound dressing with reliable hemostatic and antibacterial capability for traumatic injuries, Adv. Healthc. Mater. 12 (25) (2023) 2300312.
[48] H. Zhao, J. Huang, Y. Li, X. Lv, H. Zhou, H. Wang, Y. Xu, C. Wang, J. Wang, Z. Liu, ROS-scavenging hydrogel to promote healing of bacteria infected diabetic wounds, Biomaterials 258 (2020) 120286.